



HAL
open science

Near-field linear sampling method for axisymmetric eddy current tomography

Housseem Haddar, Mohamed Kamel Riahi

► **To cite this version:**

Housseem Haddar, Mohamed Kamel Riahi. Near-field linear sampling method for axisymmetric eddy current tomography. *Inverse Problems*, 2021, 37 (10), pp.105002. 10.1088/1361-6420/ac1c50 . hal-03517989

HAL Id: hal-03517989

<https://inria.hal.science/hal-03517989>

Submitted on 8 Jan 2022

HAL is a multi-disciplinary open access archive for the deposit and dissemination of scientific research documents, whether they are published or not. The documents may come from teaching and research institutions in France or abroad, or from public or private research centers.

L'archive ouverte pluridisciplinaire **HAL**, est destinée au dépôt et à la diffusion de documents scientifiques de niveau recherche, publiés ou non, émanant des établissements d'enseignement et de recherche français ou étrangers, des laboratoires publics ou privés.

Near-Field Linear Sampling Method for Axisymmetric Eddy Current Tomography

Housseem HADDAR¹ and Mohamed Kamel RIAHI^{2,3†}

¹ INRIA, Ecole Polytechnique (CMAP), Université Saclay Ile de France, Route de Saclay, 91128 Palaiseau, France

E-mail: haddar@cmap.polytechnique.fr

² Department of Mathematics, Khalifa University of Sciences and Technology, P.O. Box 127788, Abu Dhabi, UAE.

E-mail: mohamed.riahi@ku.ac.ae

³ Emirates Nuclear Technology Center (ENTC), Khalifa University of Science and Technology, UAE

Abstract. This paper is concerned with Eddy-Current (EC) nondestructive testing of conductive materials and focuses, in particular, on extending the well-known Linear Sampling Method (LSM) to the case of EC equations. We first present the theoretical foundation of the LSM in the present context and in the case of point sources. We then explain how this method can be adapted to a realistic setting of EC probes. In the case of identifying the shape of external deposits from impedance measurements taken from inside of the tube (steam generator), we show how the method can be applied to measurements obtained from a sweeping set of coils. Numerical experiments suggest that good results can be achieved using only a few coils and even in the limiting case of backscattering data.

Keywords: Eddy-current, Impedance measurement, Inverse imaging, non destructive testing.

1. Introduction

We investigate the application of the so-called Linear Sampling Method (LSM) [8, 7, 4, 20] to identify conductive inclusions using eddy current probes. We specifically treat the axisymmetric case motivated by the non destructive testing of tubes with axisymmetric coils. This setting corresponds for instance with the inspection of tubes used in steam generators of nuclear power plants for circulating hot water to produce steams (which is then used by a turbine to produce electricity) [10]. One then is interested in detecting and evaluating the amount of magnetite deposits on the outer parts of the tube using coils that can be inserted inside the tubes [25, 15, 21]. Given the high number of tubes, axisymmetric probes (usually referred to as SAX probes)

are used in the inspection campaign that requires shutting down the power plant and evacuating the water circulating inside the steam generator.

Given the frequency range of the probes and the conductivity of the tube and the deposits, eddy current model is adapted to describe the measurements. In general, only back-scattering or nearly back-scattering data is measured. This is why mainly optimization like methods have been used in the literature to tackle the inherent inverse problem [12, 23, 14, 16, 3]. In a perspective of studying other measurement settings or provide existing ones with good initial guess, we investigate here the performance of LSM for various measurements configurations.

We refer to [5, 6] and references therein for an overview of wider use of eddy currents in non destructive testings. Inverse shape problems for eddy current models have been studied in different contexts and using different methodologies in [26, 1, 17, 18] that may also be of interest for the application considered here.

We first analyze the idealistic case where coils can be approximated by point sources and measurements can be modeled as point-wise values of the scattered field. We formalize this setting in an axisymmetric configuration of the medium and for the eddy current model. Our analysis of the forward problem follows [11, 2]. We then study the theoretical foundations of the LSM in the case where the deposit is characterized by a change in the conductivity with respect to a reference configuration. The measurements and sources are supposed to lie on an infinite line parallel to the axis of symmetry. Observing that the spread of the incident field is limited to a narrow area surrounding the source location, the multi-static measurement matrix is almost band limited (the entries outside some few diagonals may be negligible). This means that numerically, replacing the full matrix by an M-diagonal matrix may lead to an error that is of the order the noise level. This suggests that a good approximation of the measurement matrix may be achieved using only a few number, say M of probes, (i.e. $(2M - 1)$ -diagonal matrix) that move together along the symmetry axis. At each position, the probes collect the measurements for a column of the matrix. This procedure corresponds with commonly used methods in practice for collecting the data. For the application mentioned above, 2 coils are used in general in SAX probes.

Motivated by these considerations we numerically explore the outcome of the LSM when the full matrix is replaced by its $(2M - 1)$ -diagonal. We observe for instance that even for $M = 1$ (i.e. back-scattering data), a reasonable localization and size estimate of the deposit are obtained. After discussing the idealistic case of point sources, we extend the numerical algorithm to realistic modelling of the coils (as extended sources) and compute the measurements using the impedance model [5] (see also [12]). The physical quantities and characteristic of the coils correspond with the one used in the application mentioned above. An extensive numerical discussion of the algorithm show the viability of our algorithm for this setting for providing quick and qualitatively accurate identification of the location, topology (number of connected components) and vertical dimensions of the deposit.

The outline of the paper is as follows. We introduce in Section 2 the physical model

and recall some known results on the well posedness of the underlying PDE model. We present in Section 3 the idealistic setting of the inverse problem corresponding with point sources. This requires in particular the introduction of the Green function for the axisymmetric problem. The theoretical foundations of the LSM are studied in Section 4. The last section is dedicated to a numerical validation of the LSM for various settings of the collected data. We start with the case of point sources then consider the case of more realistic models that correspond to SAX probes.

2. Preambles

Consider a simply-connected domain $\Omega \subset \mathbb{R}^3$ with Lipschitz boundary. For a given applied divergence free electric current density \mathbf{J} , a frequency ω , a magnetic permeability $\mu > 0$ and an electric conductivity $\sigma \geq 0$, the time harmonic eddy-current equations for the electric field \mathbf{E} can be formulated as

$$\mathbf{curl} \left(\frac{1}{\mu} \mathbf{curl} \mathbf{E} \right) - i\omega\sigma\mathbf{E} = i\omega\mathbf{J} \quad \text{in } \mathbb{R}^3 \quad (1)$$

supplemented with an appropriate gauge conditions for the divergence of the electric field [24, 22]. Motivated by non destructive inspection of long tubes, we here consider the axi-symmetric configuration where all quantities are invariant with respect to \mathbf{e}_θ where $(\mathbf{e}_r, \mathbf{e}_\theta, \mathbf{e}_z)$ denotes the canonical basis of the cylindrical coordinate system. We further assume that $\mathbf{J} = J\mathbf{e}_\theta$ with J independent from the θ coordinate. Then the electric field is azimuthal: $\mathbf{E} = E_\theta\mathbf{e}_\theta$ and satisfies

$$\frac{\partial}{\partial r} \left(\frac{1}{\mu r} \frac{\partial}{\partial r} (rE_\theta) \right) + \frac{\partial}{\partial z} \left(\frac{1}{\mu} \frac{\partial}{\partial z} E_\theta \right) + i\omega\sigma E_\theta = -i\omega J \quad \text{in } \mathbb{R}_+^2, \quad (2)$$

with $\mathbb{R}_+^2 := \{(r, z) : r > 0, z \in \mathbb{R}\}$. Due to symmetry, we also have

$$E_\theta|_{r=0} = 0,$$

and we impose a decay condition

$$E_\theta \rightarrow 0 \quad \text{as } r^2 + z^2 \rightarrow +\infty,$$

that models radiation condition at infinity. For a variational study of this problem we refer to [11] and we shall outline in the sequel the main result. Let $\xi > 1$ be a fixed parameter. For functions of the variables (r, z) we shall use in the following the short notation $\nabla := (\partial_r, \partial_z)^T$ to refer to the gradient with respect to these two variables. We then define the weighted functional spaces

$$L_\xi^2(\Omega) := \{v \text{ measurable} \mid \sqrt{r/(1+r^2)^\xi} v \in L^2(\Omega)\},$$

and

$$V_\xi(\Omega) := \{v \in L_\xi^2(\Omega) \mid \nabla(rv)/\sqrt{r} \in L^2(\Omega)\}.$$

The direct problem can then be stated as seeking $E_\theta = u \in V_\xi(\mathbb{R}_+^2)$ such that

$$\nabla \cdot \left(\frac{1}{\mu r} \nabla(ru) \right) + i\omega\sigma u = -i\omega J \quad \text{in } \mathbb{R}_+^2, \quad (3)$$

We observe that the boundary condition at $r = 0$ and the decay at infinity are automatically included into the solution space. This problem is equivalent to the variational form: $u \in V_\xi(\mathbb{R}_+^2)$

$$\int_{\mathbb{R}_+^2} \frac{1}{\mu r} \nabla(ru) \cdot \nabla(r\bar{v}) \, dr \, dz - \int_{\mathbb{R}_+^2} i\omega\sigma u \bar{v} \, dr \, dz = \ell(v) \quad \forall v \in V_\xi(\mathbb{R}_+^2), \quad (4)$$

with

$$\ell(v) = \int_{\mathbb{R}_+^2} i\omega J \bar{v} r \, dr \, dz$$

We then have the following Theorem [11] (see also [2]).

Theorem 1. *Assume that μ and σ are in $L^\infty(\mathbb{R}_+^2)$ and that $\mu(r, z) \geq \mu_* > 0$ on \mathbb{R}_+^2 and $\sigma = 0$ for $r \geq r^*$ sufficiently large. Consider a source term $v \mapsto \ell(v)$ that is antilinear and continuous on $V_\xi(\mathbb{R}_+^2)$. Then, the variational problem (4) admits a unique solution $u \in V_\xi(\mathbb{R}_+^2)$.*

3. Setting of the inverse problem for point sources

We discuss in this section the inverse problem for an idealized configuration where the sources J produced by coils can be considered as point sources. These sources are distributed on

$$\Gamma_s = \{ \mathbf{r} = (r, z) \in \mathbb{R}_+^2 \mid r = r_s \}$$

that we shall assume to be located in a non conductive part (here r_s is fixed). The reference domain (i.e. the domain that does not contain defects) is described by a conductivity σ_0 and a permeability μ_0 that satisfy the assumption of Theorem 1 and for simplicity we also assume that they are independent from the variable z . Let us introduce the Green function $\mathcal{G}(\cdot, \mathbf{r}_0)$ associated with a point source at $\mathbf{r}_0 = (r_0, z_0)$ satisfying

$$\nabla \frac{1}{r} \cdot \nabla r \mathcal{G}(\cdot, \mathbf{r}_0) = -\delta_{\mathbf{r}_0}(\cdot) \quad \text{in } \mathbb{R}_+^2 \quad (5)$$

with homogeneous Dirichlet boundary conditions at $r = 0$ and which is vanishing at $+\infty$. Noticing that (for θ being the angle of polar-coordinate system) the function $\Phi(x, y, z) := \mathcal{G}(\mathbf{r}, \mathbf{r}_0) \sin \theta$ satisfies $\Delta \Phi = -\sin \theta \delta_{\mathbf{r}_0}$ in \mathbb{R}^3 with a decaying condition at infinity. It is, therefore, possible to derive an integral representation of $\mathcal{G}(\cdot, \mathbf{r}_0)$ using the fundamental solution of the Laplace operator in \mathbb{R}^3 , namely [22]

$$\mathcal{G}(\mathbf{r}, \mathbf{r}_0) = \frac{1}{4\pi} \int_0^{2\pi} \frac{r_0 \sin \theta'}{|r^2 + r_0^2 - 2rr_0 \sin \theta' + |z - z_0|^2|^{1/2}} \, d\theta' \quad (6)$$

It has been shown in [9] that this integral can be analytically identified as

$$\mathcal{G}(\mathbf{r}, \mathbf{r}_0) = \frac{1}{2\pi} \sqrt{\frac{r_0}{r}} Q_{1/2} \left(1 + \frac{|\mathbf{r} - \mathbf{r}_0|^2}{2rr_0} \right) \quad (7)$$

where Q_ν is the Legendre function of the second kind, satisfying

$$(1 - t^2)Q_\nu''(t) - 2tQ_\nu'(t) + \nu(1 + \nu)Q_\nu(t) = 0.$$

The asymptotic behavior of $Q_\nu(t)$ for large argument shows that $Q_{1/2}(t) \sim \frac{\pi}{\sqrt{32}} t^{-3/2}$, therefore

$$\mathcal{G}(\mathbf{r}, \mathbf{r}_0) \sim \frac{r_0^2 r}{4|\mathbf{r}|^3} \quad \text{as } |\mathbf{r}| \rightarrow \infty$$

and

$$\mathcal{G}(\mathbf{r}, \mathbf{r}_0) \sim \frac{r_0^2 r}{4(r^2 + r_0^2 + |z - z_0^2|)^{3/2}} \quad \text{as } r \rightarrow 0.$$

This function allows us to define an incident field associated with a point source $\mathbf{r}_0 \in \Gamma_s$ as the function $u^0(\cdot, \mathbf{r}_0)$ satisfying

$$\nabla \frac{1}{\mu_0 r} \cdot \nabla r u^0(\cdot, \mathbf{r}_0) + i\omega \sigma_0 u^0(\cdot, \mathbf{r}_0) = -\delta_{\mathbf{r}_0}(\cdot) \quad \text{in } \mathbb{R}_+^2 \quad (8)$$

with homogeneous Dirichlet boundary conditions at $r = 0$ and which is vanishing at $+\infty$. This function can be constructed as

$$u^0(\cdot, \mathbf{r}_0) = \mu_0(\mathbf{r}_0) \mathcal{G}(\cdot, \mathbf{r}_0) + \tilde{u}^0(\cdot, \mathbf{r}_0) \quad (9)$$

where $\tilde{u}^0(\cdot, \mathbf{r}_0) \in V_\xi(\mathbb{R}_+^2)$ and is the unique solution of (4) with $\mu = \mu_0$, $\sigma = \sigma_0$ and

$$\ell(v) = \int_{\mathbb{R}_+^2} \left(1 - \frac{\mu_0(\mathbf{r}_0)}{\mu_0(\mathbf{r})} \right) \nabla r \mathcal{G}(\mathbf{r}, \mathbf{r}_0) \cdot \nabla r \bar{v}(\mathbf{r}) \, d\mathbf{r} + \int_{\mathbb{R}_+^2} i\omega \sigma_0 \mu_0(\mathbf{r}_0) \mathcal{G}(\mathbf{r}, \mathbf{r}_0) \bar{v}(\mathbf{r}) r \, d\mathbf{r}.$$

We now consider the inverse problem configuration for the imaging of deposits inside the reference media defined by μ_0 and σ_0 . We assume that this deposit occupies a domain D that lies in the region $r_s < r < r_* < \infty$.

Remark 1. *It is worth noticing that studying the case of deposit in the region $D \subset \{r < r_s\}$ follows the same lines as in the case studied here. In the Engineering application we have in mind magnetite deposits occur in the outer shell side of the tube.*

Let us denote by μ and σ the functions defining the material properties of the domain with deposit. In particular $\mu = \mu_0$ and $\sigma = \sigma_0$ outside D .

The probes are point sources located at $\mathbf{r}_0 \in \Gamma_s$, that generate a field $u(\cdot, \mathbf{r}_0)$ satisfying

$$\nabla \frac{1}{\mu r} \cdot \nabla r u(\cdot, \mathbf{r}_0) + i\omega \sigma u(\cdot, \mathbf{r}_0) = -\delta_{\mathbf{r}_0}(\cdot) \quad \text{in } \mathbb{R}_+^2 \quad (10)$$

with homogeneous Dirichlet boundary conditions at $r = 0$ and which is vanishing at $+\infty$. The field function can be defined as

$$u(\cdot, \mathbf{r}_0) = u^0(\cdot, \mathbf{r}_0) + u^s(\cdot, \mathbf{r}_0)$$

where $u^s(\cdot, \mathbf{r}_0) \in V_\xi(\mathbb{R}_+^2)$ is the scattered field that can be defined as the unique solution of (4) with

$$\ell(v) = \int_D \left(\frac{1}{\mu_0(\mathbf{r})} - \frac{1}{\mu(\mathbf{r})} \right) \nabla r u^0(\mathbf{r}, \mathbf{r}_0) \cdot \nabla r \bar{v}(\mathbf{r}) \, d\mathbf{r} - \int_D i\omega(\sigma_0 - \sigma) u^0(\mathbf{r}, \mathbf{r}_0) \bar{v}(\mathbf{r}) r \, d\mathbf{r}. \quad (11)$$

Since the deposit D does not intersect Γ_s , we clearly have that $u^0(\cdot, \mathbf{r}_0) \in V_\xi(D)$ and therefore this antilinear form is continuous on $V_\xi(\mathbb{R}_+^2)$. This guarantees by application of Theorem 1 the existence and uniqueness of $u^s(\cdot, \mathbf{r}_0) \in V_\xi(\mathbb{R}_+^2)$. Using a test function $\bar{v}(\mathbf{r}') = u^0(\mathbf{r}', \mathbf{r})$ and integrating by parts leads to the following representation theorem.

Proposition 1. *The scattered field $u^s(\cdot, \mathbf{r}_0)$ defined above satisfies for $r_0, r > 0$ the reciprocity relation $ru^s(\mathbf{r}, \mathbf{r}_0) = r_0 u^s(\mathbf{r}_0, \mathbf{r})$ as well as the integral representation*

$$\begin{aligned} ru^s(\mathbf{r}, \mathbf{r}_0) &= \int_D \left(\frac{1}{\mu_0(\mathbf{r}')} - \frac{1}{\mu(\mathbf{r}')} \right) \nabla(r' u^0(\mathbf{r}', \mathbf{r})) \cdot \nabla(r' u(\mathbf{r}', \mathbf{r}_0)) \, d\mathbf{r}' \quad (12) \\ &\quad + i\omega \int_D (\sigma - \sigma^0) u(\mathbf{r}', \mathbf{r}_0) u^0(\mathbf{r}', \mathbf{r}) r' \, d\mathbf{r}'. \end{aligned}$$

It is worth noticing that the reciprocity relation is also satisfied by $\mathcal{G}(\cdot, \cdot)$ as well as $u^0(\cdot, \cdot)$.

The inverse problem we would like to address first is the problem of reconstructing D from measurements of $u^s(\mathbf{r}, \mathbf{r}_0)$ for all \mathbf{r} and \mathbf{r}_0 in Γ_s using the so-called Linear Sampling Method. We shall later explain how this method can provide an inversion method for realistic setting (related to non destructive testing of conducting tubes) using few eddy-current coils (and even back-scattering configurations).

A key ingredient in the justification of the method is the following unique continuation argument associated with measurements.

Theorem 2. *Let D be a bounded domain in the region $r > r_s$ with connected complement in \mathbb{R}_+^2 . Let u_1 and u_2 in $V_\xi(\mathbb{R}_+^2 \setminus \bar{D})$ and satisfy*

$$\nabla \frac{1}{\mu_0 r} \cdot \nabla r u_i + i\omega \sigma_0 u_i = 0 \quad \text{in } \mathbb{R}_+^2 \setminus \bar{D}. \quad (13)$$

If $u_1 = u_2$ on Γ_s , then $u_1 = u_2$ in $\mathbb{R}_+^2 \setminus D$.

Proof. Denoting $\Omega := \{\mathbf{r}, 0 < r < r_s\}$, we observe that $v = u_1 - u_2 \in V_\xi(\Omega) \cap H_0^1(\Omega)$ and verifies the variational formulation (4) with $\mu = \mu_0$, $\sigma = \sigma_0$, $\ell = 0$ and $V_\xi(\mathbb{R}_+^2)$ replaced with $V_\xi(\Omega) \cap H_0^1(\Omega)$. The coercivity of the associated sesquilinear form in $V_\xi(\Omega) \cap H_0^1(\Omega)$ implies that $u_1 = u_2$ in Ω . We then conclude that $u_1 = u_2$ in $\mathbb{R}_+^2 \setminus D$ using classical unique continuation argument for elliptic second order operators with piecewise constant coefficients (with Lipschitz interfaces). \square

4. Foundations of the linear sampling method and algorithm

The extension of the linear sampling method to the current setting does not raise major difficulties or differences with respect to the classical setting of method for inverse

scattering problem [8, 7, 4]. This is why we shall give in the following only the outline of this method and eventually the key points of the proofs. The assumptions made in the previous section for σ , σ_0 , μ and μ_0 so that the forward problems defining $u^0(\cdot, \mathbf{r}_0)$ and $u(\cdot, \mathbf{r}_0)$ are well posed are assumed to hold true and we will not further indicate that in the subsequent theorems or results.

To simplify the technical details we further assume here that $\mu = \mu_0$ and therefore the deposit is characterized only by variation of the conductivity value σ .

We introduce the measurement operator \mathcal{Z} as follows:

$$\mathcal{Z} : L^2(\Gamma_s) \longrightarrow L^2(\Gamma_s) \quad (14)$$

$$g \longmapsto (\mathcal{Z}g)(\mathbf{r}) := \int_{\Gamma_s} u^s(\mathbf{r}, \mathbf{r}_0)g(\mathbf{r}_0) ds(\mathbf{r}_0) \quad \mathbf{r} \in \Gamma_s \quad (15)$$

The linearity of u^s with respect to u^0 shows that $\mathcal{Z}g$ corresponds with the trace of u_g^s on Γ_s where $u_g^s \in V_\xi(\mathbb{R}_+^2)$ is the unique solution of (4) with source term ℓ defined by (11) where u^0 is replaced by the single layer potential

$$v_g^0(\mathbf{r}) = \int_{\Gamma_s} u^0(\mathbf{r}, \mathbf{r}_0)g(\mathbf{r}_0) ds(\mathbf{r}_0). \quad (16)$$

We then have a natural decomposition of the measurement operator as

$$\mathcal{Z} = \mathcal{G} \circ \mathcal{S}$$

where the operator $\mathcal{S} : L^2(\Gamma_s) \rightarrow L^2(D)$ is defined by $\mathcal{S}g := v_g^0|_D$ and where the solution operator $\mathcal{G} : L^2(D) \rightarrow L^2(\Gamma_s)$ is defined by $\mathcal{G}(v) = w|_{\Gamma_s}$ with $w \in V_\xi(\mathbb{R}_+^2)$ being the unique solution of (4) with source term ℓ defined by (11) replacing u^0 by the function $v \in L^2(D)$. We first prove the following important properties of the operator \mathcal{S} .

Lemma 3. *The operator $\mathcal{S} : L^2(\Gamma_s) \rightarrow L^2(D)$ is injective. The range of this operator is dense in*

$$V_g(D) := \left\{ v \in L^2(D), \quad \nabla \frac{1}{\mu_0 r} \cdot \nabla r v + i\omega\sigma_0 v = 0, \text{ in } D \right\}. \quad (17)$$

Proof. We first prove the injectivity. We observe that according to (6) and the preceding discussion, if we set $g \in L^2(\Gamma_s)$

$$SL(g)(\mathbf{r}) := \int_{\Gamma_s} \mathcal{G}(\mathbf{r}, \mathbf{r}_0)g(\mathbf{r}_0) ds(\mathbf{r}_0).$$

then

$$SL(g)(\mathbf{r}) \sin(\theta) = \int_{\Gamma_s \times [0, 2\pi]} \frac{\tilde{g}(\mathbf{x}_0)}{4\pi|\mathbf{x} - \mathbf{x}_0|} ds(\mathbf{x}_0) \quad (18)$$

where $\mathbf{x} = (r \cos \theta, r \sin \theta, z)$, $\mathbf{x}_0 = (r_0 \cos \theta', r_0 \sin \theta', z_0)$ and $\tilde{g}(\mathbf{x}_0) = g(\mathbf{r}_0) \sin \theta'$. This remark allows us to deduce that $SL(g)$ has the same continuity properties across Γ_s as the single layer potential associated with Laplace operator in \mathbb{R}^3 [19]. In particular $SL(g)$ is continuous across Γ_s while its normal derivative (derivative with respect to r

here) has a jump across Γ_s equals to $-g$. Given the decomposition (9) of $u_0(\cdot, \mathbf{r}_0)$ and the fact that $\tilde{u}_0(\cdot, \mathbf{r}_0)$ is regular in the neighborhood of Γ_s , one deduces that v_g^0 has the same continuity properties as $SL(g)$ across Γ_s . Now assume that $\mathcal{S}g = 0$. This implies that $v_g^0 = 0$ in D . Since v_g^0 satisfies

$$\nabla \frac{1}{\mu_0 r} \cdot \nabla r v_g^0 + i\omega \sigma_0 v_g^0 = 0 \quad \text{in } \mathbb{R}_+^2 \setminus \Gamma_s. \quad (19)$$

we deduce, using classical unique continuation arguments for elliptic second order operators with piecewise constant coefficients, that $v_g^0 = 0$ for $r > r_s$. This implies in particular that $v_g^0 = 0$ on Γ_s . Following the same reasoning as in the proof of Theorem 2, we then deduce that $v_g^0 = 0$ for $0 < r < r_s$ since it satisfies the homogeneous Dirichlet problem in the region $0 < r < r_s$. The jump properties of the normal derivative of across Γ_s finally implies that $g = 0$ which conclude the proof of injectivity. For the denseness of the range, it is sufficient to prove that the adjoint operator \mathcal{S}^* is injective on $V_g(D)$. It is natural to consider the adjoint with respect to the duality product $\int_D f(\mathbf{r})g(\mathbf{r}')r d\mathbf{r}$, in which case

$$\mathcal{S}^*v(\mathbf{r}_0) = \int_D u^0(\mathbf{r}, \mathbf{r}_0)v(\mathbf{r})r d\mathbf{r}$$

Denote by $r_0w(\mathbf{r}_0)$ the function defined by the right hand side for $\mathbf{r}_0 \in \mathbb{R}_+^2$. We then have $w \in V_\xi(\mathbb{R}_+^2)$ and satisfies (similarly to the statement in Proposition 1

$$\nabla \frac{1}{\mu_0 r} \cdot \nabla r w + i\omega \sigma_0 w = -\bar{v}|_D \quad \text{in } \mathbb{R}_+^2 \quad (20)$$

with Dirichlet boundary condition at $r = 0$. Assuming that $\mathcal{S}^*v = 0$ implies that w vanishes on Γ_s and by Theorem 2, $w = 0$ in $\mathbb{R}_+^2 \setminus D$. Multiplying (20) with rv and integrating over D implies after applying the Green Theorem twice (this can be justified using a density argument)

$$\int_D |v|^2 r d\mathbf{r} = \int_D w \left(\nabla \frac{1}{\mu_0 r} \cdot \nabla r v + i\omega \sigma_0 v \right) r d\mathbf{r} = 0$$

which implies $v = 0$ and concludes the proof. \square

The study of LSM for penetrable media requires the analysis of so-called interior transmission problems (ITP). In our context this problem can be formulated as: seek $(w, v) \in H^2(D) \times L^2(D)$ such that

$$\begin{cases} \nabla \frac{1}{\mu_0 r} \cdot \nabla r w + i\omega \sigma w = -i\omega(\sigma - \sigma_0)v & \text{in } D \\ \nabla \frac{1}{\mu_0 r} \cdot \nabla r v + i\omega \sigma_0 v = 0 & \text{in } D \\ w = f & \text{on } \partial D \\ \frac{\partial w}{\partial \mathbf{n}} = h & \text{on } \partial D \end{cases} \quad (\text{ITP})$$

where $f \in H^{3/2}(\partial D)$ and $h \in H^{1/2}(\partial D)$. The well posedness of this problem is an essential assumption for the following arguments justifying the Linear Sampling method.

Let us remark that since we assume that D is bounded and does not touch $r = 0$, the study of this problem follows the same lines as the study of the well posedness of this problem where the operator $\nabla \frac{1}{\mu_0 r} \cdot \nabla r$ is replaced with the operator Δ . For instance this problem is of Fredholm type as long as $\sigma - \sigma_0$ is positive definite or negative definite in a neighborhood of the boundary of D . The uniqueness of solution can be established for all ω if one assumes that $\sigma_0|_D = 0$ and $\sigma|_D = 0$ is positive. The study of (ITP) in the case where D touches $r = 0$ or in the case where the domain is unbounded may require additional arguments than those classically used in [7]. A detailed discussion of these issues are out of the scope of this work and may be the subject of a future work. For the present case we restrict ourselves to assuming that ω , μ_0 , σ and σ_0 are such that (ITP) admits a unique solution.

For a given point $\boldsymbol{\xi}$ in \mathbb{R}_+^2 , we denote by $\phi_{\boldsymbol{\xi}} \in L^2(\Gamma_s)$ the function defined by

$$\phi_{\boldsymbol{\xi}}(\mathbf{r}) := u^0(\mathbf{r}, \boldsymbol{\xi}) \quad \mathbf{r} \in \Gamma_s$$

Theorem 4. *Assume that (ITP) is well posed. Then the operator \mathcal{G} is injective on $V_g(D)$. Moreover, the equation $\mathcal{G}(v) = \phi_{\boldsymbol{\xi}}$ admits a solution $v \in V_g(D)$ if and only if $\boldsymbol{\xi} \in D$.*

Proof. Using the unique continuation argument of Theorem 2 and the fact that $u^0(\cdot, \boldsymbol{\xi}) \notin H^1(\mathbb{R}_+^2 \setminus \overline{D})$ if $\boldsymbol{\xi} \notin D$, the proof of this theorem follows the same arguments as in [7]. We here outline the main arguments. If $\mathcal{G}(v) = 0$ then by Theorem 2, this is equivalent to the existence of a solution to the homogeneous interior transmission problem (ITP). This implies that $v = 0$. If $\boldsymbol{\xi} \in D$, the existence of a solution to $\mathcal{G}(v) = \phi_{\boldsymbol{\xi}}$ is ensured by the existence of a solution to (ITP) with

$$f := u^0(\mathbf{r}, \boldsymbol{\xi})|_{\Gamma_s} \quad h := \frac{\partial u^0(\mathbf{r}, \boldsymbol{\xi})}{\partial \mathbf{n}}|_{\Gamma_s}.$$

If $\boldsymbol{\xi} \notin D$ then 2 ensures that $w = u^0(\cdot, \boldsymbol{\xi})$ in $\mathbb{R}_+^2 \setminus \overline{D}$ which contradicts the fact that $u^0(\cdot, \boldsymbol{\xi}) \notin H^1(\mathbb{R}_+^2 \setminus \overline{D})$. \square

As a corollary of Theorem 3 and Theorem 4, we obtain the following Theorem.

Theorem 5. *Assume that (ITP) is well posed. then the operator \mathcal{Z} is injective with dense range. Moreover, the following holds.*

- If $\boldsymbol{\xi} \in D$, then there exists a sequence g^ϵ such that $\|\mathcal{Z}g^\epsilon - \phi_{\boldsymbol{\xi}}\|_{L^2(\Gamma_s)} \rightarrow 0$ as $\epsilon \rightarrow 0$ and $\lim_{\epsilon \rightarrow 0} \|\mathcal{S}g^\epsilon\|_{L^2(D)} < +\infty$.
- If $\boldsymbol{\xi} \notin D$ then for any sequence g_ϵ such that $\|\mathcal{Z}g_\epsilon - \phi_{\boldsymbol{\xi}}\|_{L^2(\Gamma_s)} \rightarrow 0$ as $\epsilon \rightarrow 0$, $\lim_{\epsilon \rightarrow 0} \|\mathcal{S}g_\epsilon\|_{L^2(D)} = +\infty$.

The proof of this theorem follows exactly the same lines as in [7, Chapter 2]. We just emphasize that the denseness of the range of \mathcal{Z} is equivalent to its injectivity thanks to the reciprocity relation in Proposition 1.

This theorem suggests to construct nearby solutions $\mathcal{Z}g_{\xi}^{\epsilon} \simeq \phi_{\xi}$ and construct an indicator for D based on some norm related to g_{ξ}^{ϵ} . In the literature, numerical experiments proved that an appropriate implementation would consist in applying a Tikhonov regularization by solving

$$\epsilon g_{\xi}^{\epsilon} + \mathcal{Z}^* \mathcal{Z} g_{\xi}^{\epsilon} = \mathcal{Z}^* \phi_{\xi}.$$

This choice is motivated by the denseness of the range of \mathcal{Z} that ensures the construction of a nearby solution. The numerical details relate to this procedure is explained in the following section as well as the adaptations made for realistic configurations.

Consider a finite number of sources \mathbf{r}_i , $i = 1, \dots, N$, equidistantly spaced on Γ_s . We use the finite element package FreeFem++[13] to generate the incident fields and scattered fields associated with these point sources and a given deposit characterized by its shape and conductivity. The problem is discretized using P1-Lagrange elements. We also use the option adaptmesh in FreeFem++ to increase the accuracy of the computations. Figure 5 indicates an example of a mesh for the computational domain. We then numerically evaluate the data matrix

$$\mathcal{Z}_{i,j} := u^s(\mathbf{r}_i, \mathbf{r}_j).$$

This data is then corrupted with a random noise of level δ as $\tilde{\mathcal{Z}}_{i,j} = (1 + \delta_{i,j})\mathcal{Z}_{i,j}$ where $\delta_{i,j}$ are complex numbers with real and imaginary parts randomly and uniformly chosen in the interval $[-\delta, \delta]$. The inversion algorithm takes this data together with the level noise δ as entries, then builds an indicator function for the deposit as follows:

- Consider a uniform sampling of the probed region (outside the tube), which is a rectangle that contains the deposit and with a height at least equal to the distance between the farthest point sources (see Figure 5 right). Consider also a sampling point ξ_{ℓ} in this region. We evaluate the the right hand side $\phi_{\ell} \in \mathbb{C}^N$ as

$$\phi_{\ell}(i) := u^0(\mathbf{r}_i, \xi_{\ell}),$$

- We compute the function $g_{\ell} \in \mathbb{C}^N$ solution of the regularized equation, namely

$$\epsilon_{\ell} g_{\ell} + \tilde{\mathcal{Z}}^* \tilde{\mathcal{Z}} g_{\ell} = \mathcal{Z}^* \phi_{\ell}. \quad (21)$$

The regularization parameter ϵ_{ℓ} is evaluated using the Morozov's principle, i.e. it is selected so that it ensures the equality

$$\|\tilde{\mathcal{Z}}g_{\ell} - \phi_{\ell}\| = \delta \|g_{\ell}\|.$$

We finally plot the indicator function $\ell \mapsto 1/\|g_{\ell}\|$. This procedure is the usually adopted method to build the criterion for sampling methods [8].

Discussion of the case of limited number of receivers.

The previous procedure requires to have N receivers (coils) which may be for practical applications hard to set up if N is large. In general only a limited number of

coils $M \ll N$ are available. For the industrial experiment mentioned earlier, these M -probes move together along the tube axis. Consequently, one has access only to $2M - 1$ sized band-diagonal of the matrix $\tilde{\mathcal{Z}}$. With regards to the spreading of the solution around the source location (Figure 4), we see that $u^s(\mathbf{r}_i, \mathbf{r}_j) \simeq 0$ if the distance between the points \mathbf{r}_i and \mathbf{r}_j is sufficiently large. Therefore, approximating $\tilde{\mathcal{Z}}$ using the $2M - 1$ diagonals can be reasonable if M is sufficiently large. In practice M can be reduced to $M = 1$ (back-scattering data) or $M = 2$ (using 2 coils and symmetries). This is why we also experiment in the following small values of M , where surprisingly good results are obtained.

Our inversion algorithm for the case of data provided with M moving coils ($M < N$) is the same as for having N coils replacing the full matrix $\tilde{\mathcal{Z}}$ by the matrix $\tilde{\mathcal{Z}}^M$ that is obtained from $\tilde{\mathcal{Z}}$ by putting 0 outside the diagonal central band of size M . More specifically, the matrix $\tilde{\mathcal{Z}}^M$ is defined by

$$\tilde{\mathcal{Z}}_{i,j}^M = \tilde{\mathcal{Z}}_{i,j} \text{ if } |i - j| \leq M \text{ and } \tilde{\mathcal{Z}}_{i,j}^M = 0 \text{ if not.}$$

Figure 1 gives an illustration of $\tilde{\mathcal{Z}}^M$ for $M = 4$ and $N = 32$.

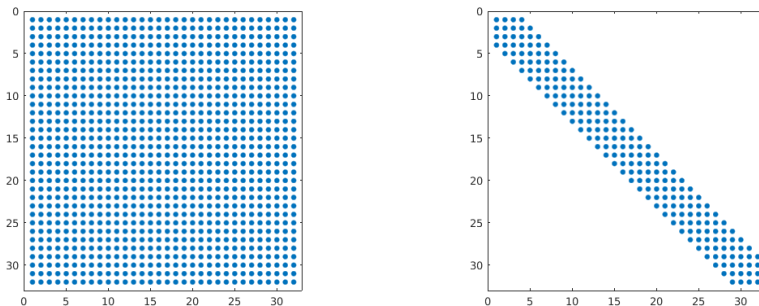


Figure 1. Profile of the non zero entries of the matrix $\tilde{\mathcal{Z}}^M$ (right) with $M = 4$ compared to the matrix $\tilde{\mathcal{Z}}$ (left).

5. Numerical experiments and validation

5.1. Description of the targeted application

The numerical experiments conducted in this section are motivated by the industrial application of identifying the shape of magnetite deposits on the external surface of tubes inside steam generators from measurements of eddy currents associated with a co-axial coil inserted inside the tube. We refer to [16, 12] for a description of the industrial context and the experimental setting. Figure 2 provides a sketch illustrating the experiment. The conductive parts are formed by the tube and the deposits.

The setting for the experiment is inspired from [16] which yields the spacing and dimensions of the coils as indicated in Figure 3.

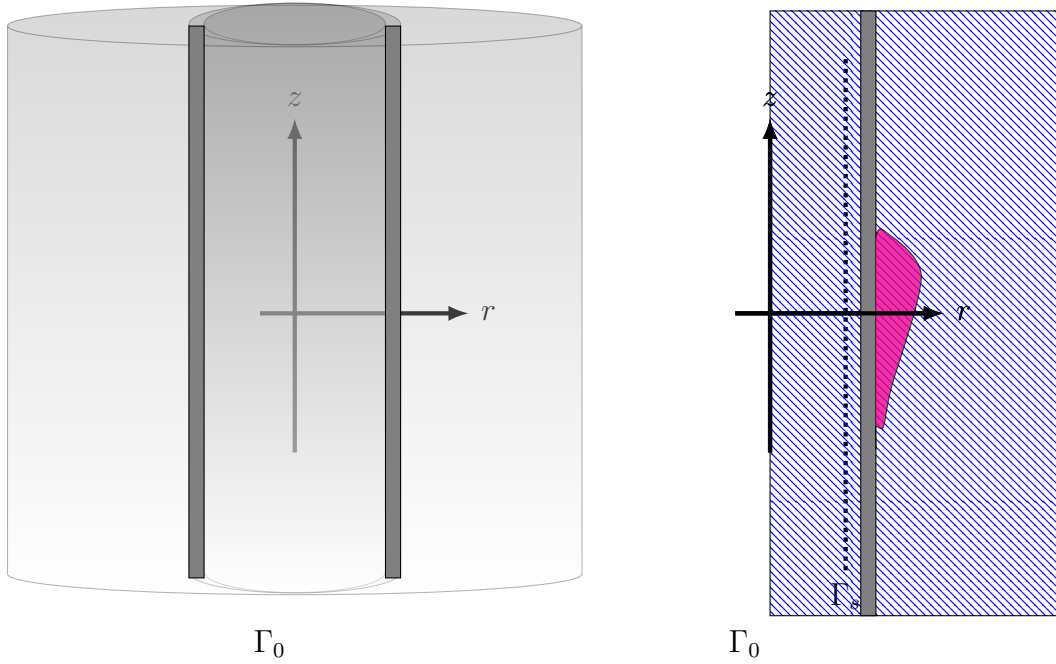


Figure 2. Configuration of the tube and its surrounding. A deposit free configuration is shown left. The right figure shows an axisymmetric cut with a deposit at the external part of the tube and the probe positions on Γ_s .

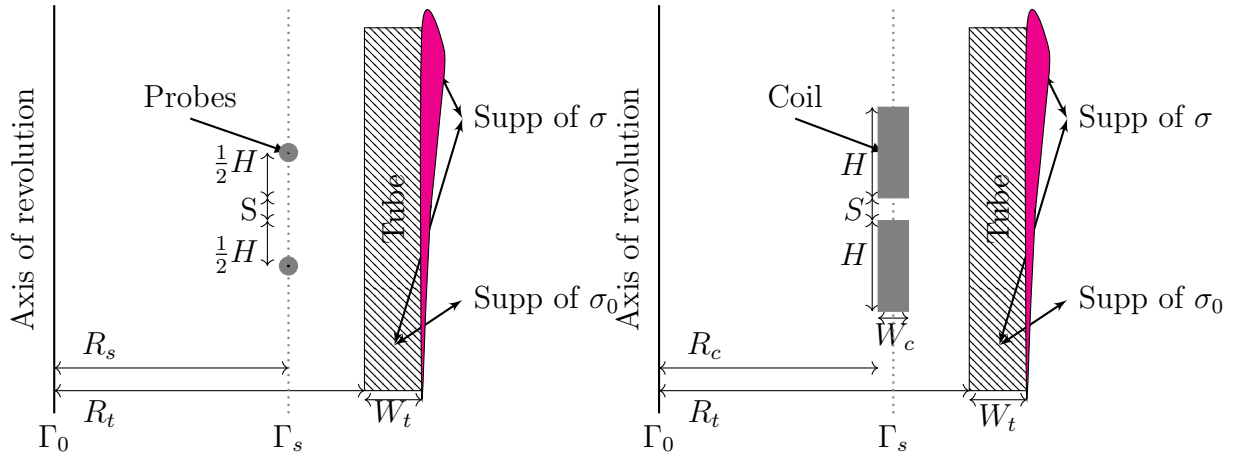


Figure 3. Sketch of the probing configuration and parameters for the sources. Right: height of the coil $H = 2\text{mm}$, width of the coil $W_c = 0.67\text{mm}$, separation between coils $S = 0.5\text{mm}$, radius of the internal boundary of the coil $R_c = 7.83\text{mm}$, internal radius of the tube $R_t = 9.84\text{mm}$ and the tube width $W_t = 1.26\text{mm}$. Left: corresponding parametrization for idealistic case of point sources. The sources are located at Γ_s with radius $R_s = 8.165\text{mm}$ which is equal to the mid radius of the coils. Successive point sources are separated by $H + S = 2.5\text{mm}$. The sketch indicates the support of σ including the defect and the support of σ_0 excluding the defect.

Figure 4 illustrates an incident field u^0 and a scattered field u^s in the case of point sources and the case of rectangular coil described in Figure 3. The scattered field correspond with two small deposits indicated by a solid line. We observe in particular the spreading of the incident field is very limited and most of the energy is captured by the two or three neighboring coils.

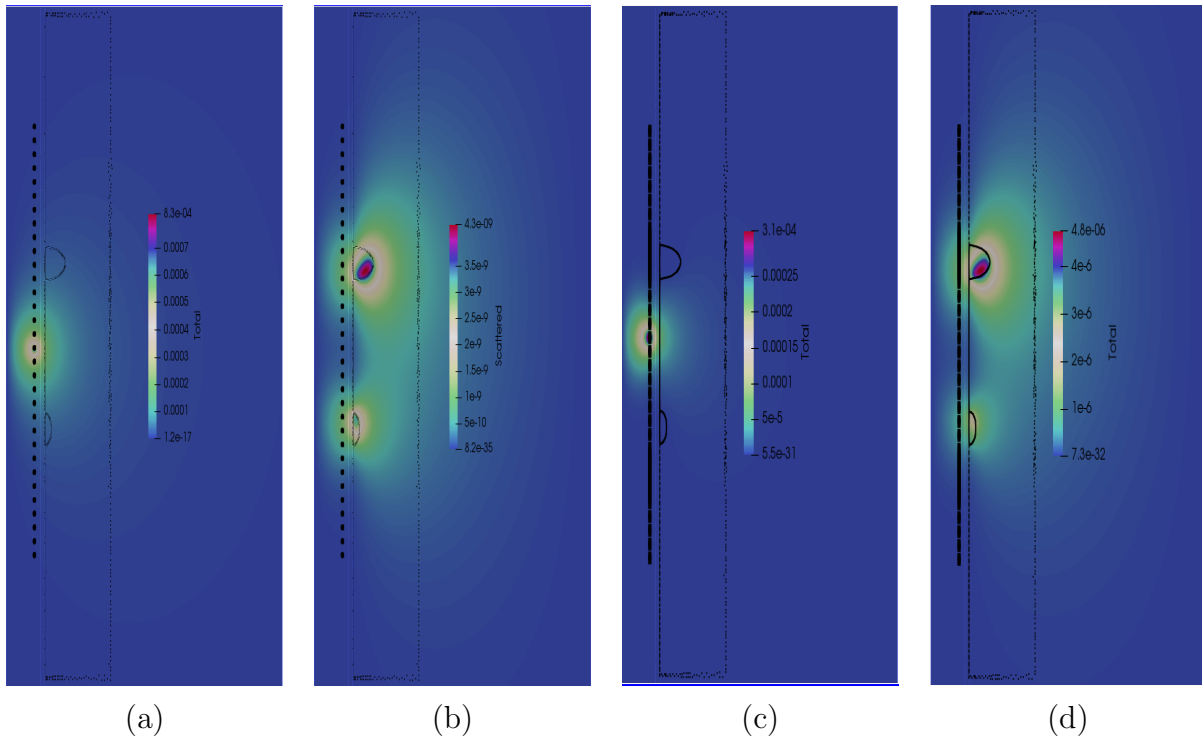


Figure 4. Eddy-current finite element solution for a frequency $\omega = 2\pi 10^5$ and two conductive deposits shaped as semi-discs distanced by about 24.5mm. From left to right: (a) total field using Green's function, (b) scattered field using point sources, (c) total field using probing coils and (d) scattered field using probing coils.

In the case of realistic experiments, only a finite number of coils are used. Moreover, the field generated by the coil is slightly different from the one generated by a point source. With this respect, we shall discuss first a validation of the model problem treated in the theoretical part when the point source approximation holds true. We then discuss how we can extend the algorithm to cases where the point source approximation does not hold.

5.2. Discussion of the inversion results in the case of point sources

We hereafter present some numerical experiments in the case of point sources. We use physical parameters compatible with the realistic configurations of the tube and deposits (see Figure 3 for geometric parameters details and Table 1 for physical details of all materials). We consider only the case of simply connected deposit while other configurations can be seen below for the case of coils.

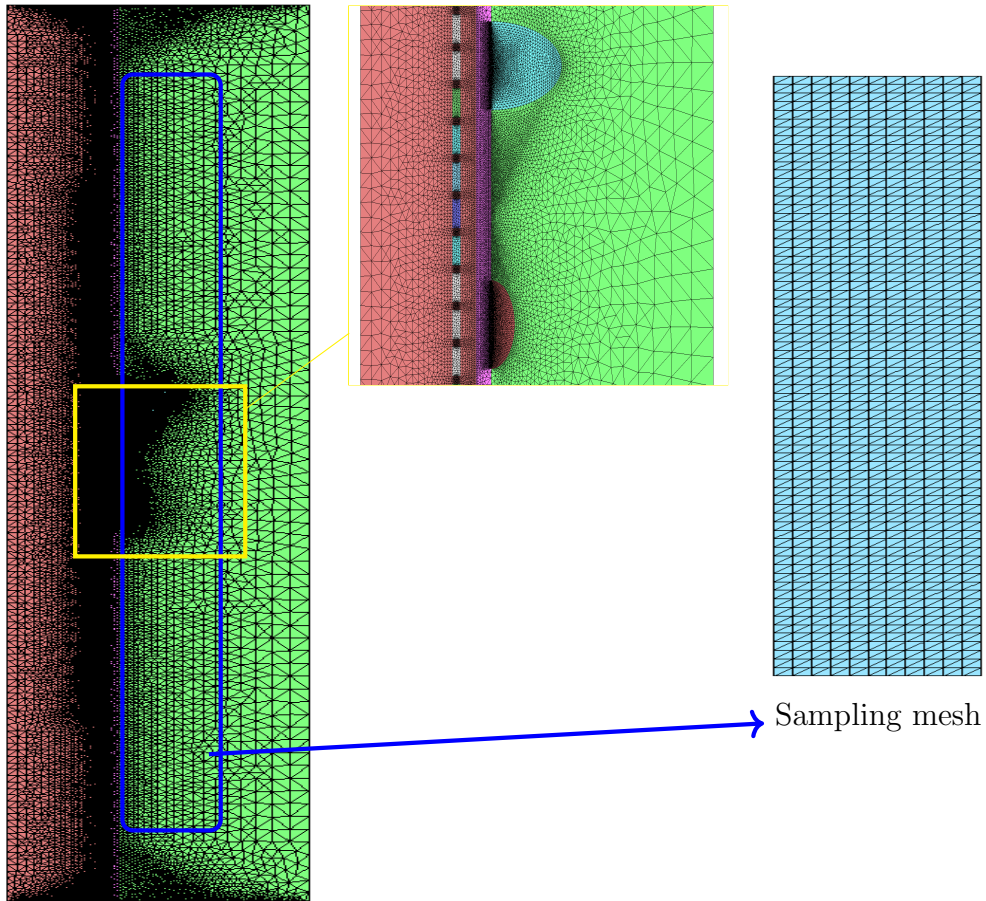


Figure 5. A typical computational mesh used for generating the data of the inverse problem. The zoomed mesh (middle) shows the mesh adaptation near conductive regions (tube + deposits) and the source location. The mesh indicated on the right of the figure is the Cartesian grid used in the probed zone to generate the sampling points of the LSM.

Example of reconstructions obtained with $\tilde{\mathcal{Z}}$ for different values of N . In this series of experiments we vary the number of sources (keeping the same vertical spacing) and use the full matrix to image the domain containing the deposit. It is observed in Figure 6 that a good accuracy is obtained with sufficiently large number of sources that covers an aperture larger than the deposit elongation. When the number of coils becomes small (4 on the left), the results indicates that a good localization maybe achieved if the sources are facing the deposit. This motivates the use of small number of coils sliding along the z direction and covering a large aperture as discussed in the following experiment.

Examples of reconstructions obtained with $\tilde{\mathcal{Z}}^M$ for different values of M . We here consider the same configuration as previously, fix $N = 32$ (this refers here to the number of positions that one point source may take) and vary the value of M which indicates the number of point sources that are sliding along the z -axis. The obtained results are illustrated by Figure 7. We observe in particular that even with back-scattering data,

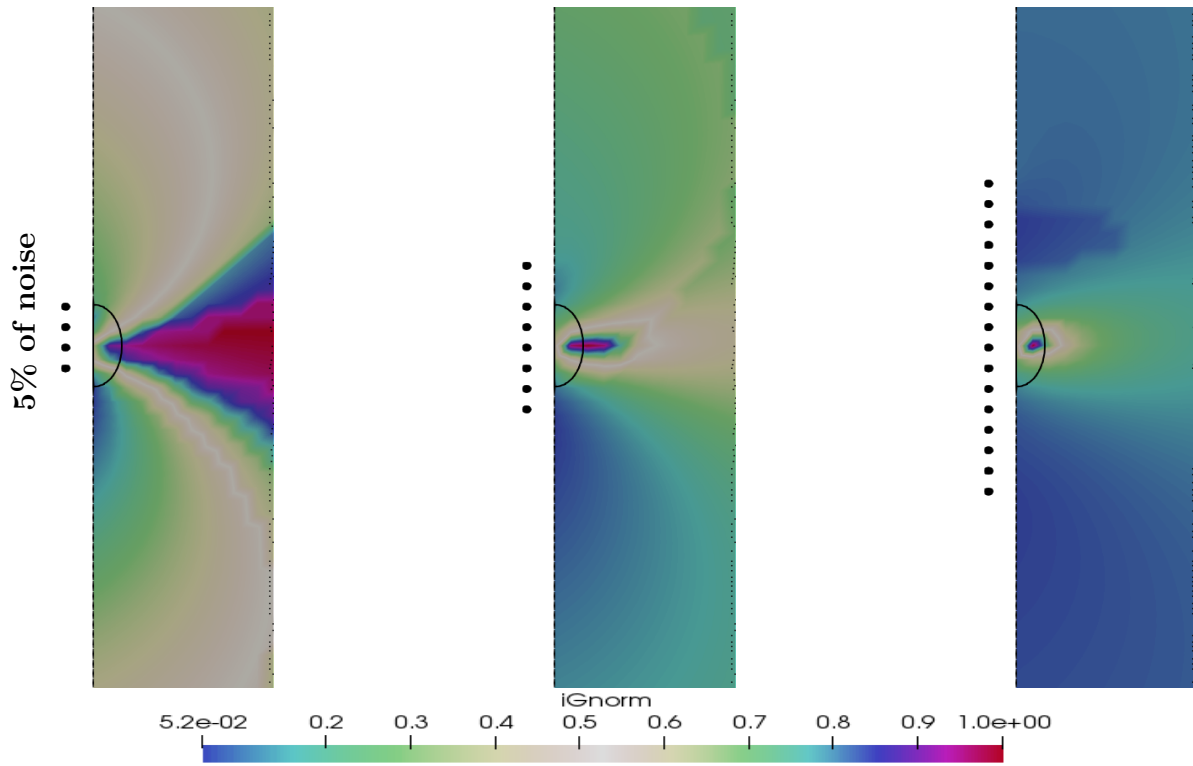


Figure 6. Reconstructions obtained for different number of point sources N . From left to right, $N = 4, 8, 16$. The location of the point sources is indicated with black small circles and the exact shape of the deposit is indicated using a solid line and it represents a semi-disc with an elliptical shape of radius 3mm in the r -direction and 5mm in the z -direction.

a good localization along the z -axis is obtained. Increasing the number of point sources improves the accuracy along the axis orthogonal to the source location.

5.3. Extension to the case of realistic coils

In real experiments the coils are better represented as volumetric sources J with constant intensity I in the region of the coil and vanishing outside. The coil region is a rectangle characterized by a center $\mathbf{r}_j \in \Gamma_s$ and dimensions H and W_c as indicated in Figure 3. Let us denote by u_j^0 and u_j the incident field and respectively the total field associated with a source J at coil position $\mathbf{r}_j \in \Gamma_s$. These fields are solutions to (3) with σ^0 and σ respectively i.e. in the absence and in the presence of a deposit. The field created by a coil at position z_j and recorded by a coil at position z_i is then given by [5, 6]

$$\mathcal{Z}_{i,j} = \frac{i\omega}{r_0} \int_D (\sigma - \sigma^0) u_i(\mathbf{r}) u_j^0(\mathbf{r}) r \, d\mathbf{r}. \quad (22)$$

This impedance has a similar structure as (12) and corresponds with averaging the scattering field over the recording coil region. Using the reciprocity relation we now design the right hand side of the sampling equation as

$$\phi_\ell(i) := u_i^0(\boldsymbol{\xi}_\ell).$$

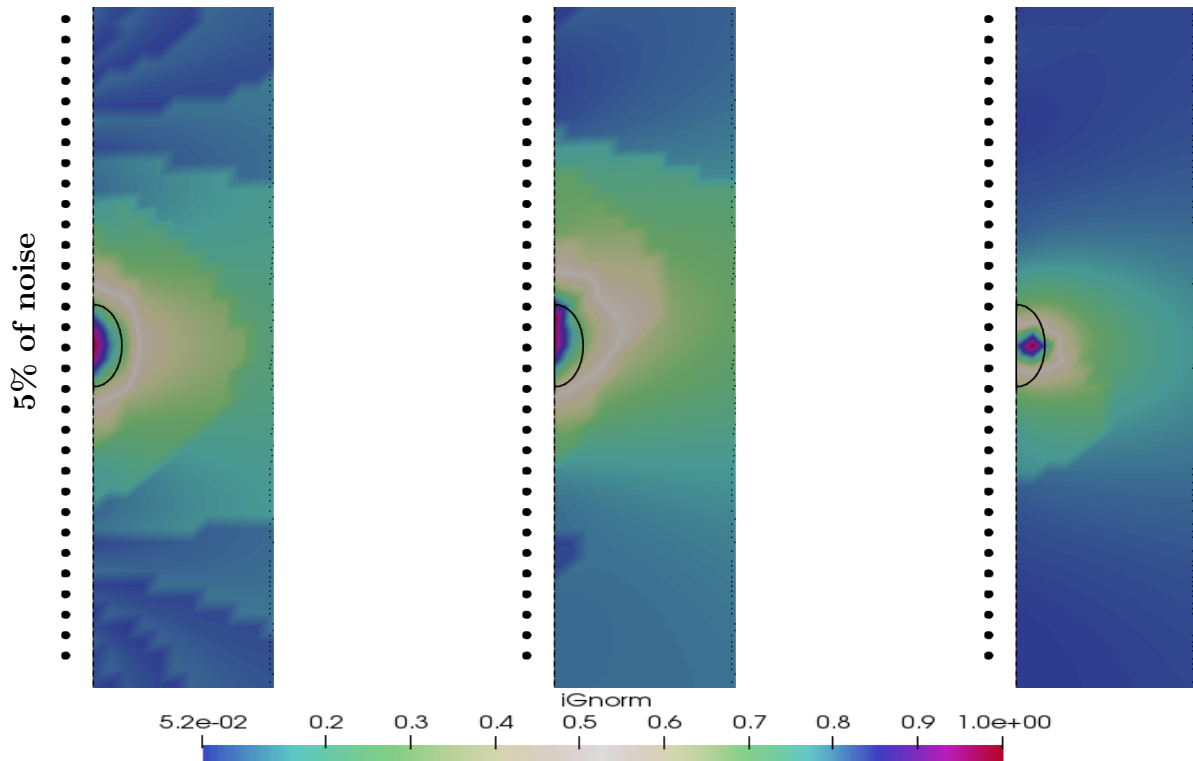


Figure 7. Reconstructions obtained with $\tilde{\mathcal{Z}}^M$ for different number of point sources M sliding along the z -axis. From left to right, $M = 1, 2, 8$. The location that can be taken by a point source is indicated with black discs ($N = 32$) and the exact shape of the deposit is indicated with a solid line and it represents a semi-disc with an elliptical shape of radius 3mm in the r -direction and 5mm in the z -direction.

The inversion algorithm is then performed the same way as in the case of point sources. In the case of a limited number of coils M , the inversion is adapted as above by replacing the noisy data $\tilde{\mathcal{Z}}$ with $\tilde{\mathcal{Z}}^M$ defined by (22).

Numerical examples. For the numerical examples below, we use realistic physical parameters related to SAX probe system, namely a coil of dimensions $0.67\text{mm} \times 2\text{mm}$ (width \times height) and a frequency $\omega = 2\pi 10^5$ Hertz. The electric conductivity and the magnetic permeability of different compartments involved in our numerical simulation are reported in table 1. We remark for instance that the skin depth $\equiv \sqrt{2/\omega\sigma\mu}$ associated with the tube is about 1.6mm and is about 1.2mm for the deposit.

Example of reconstructions obtained with $\tilde{\mathcal{Z}}$ for different values of N . As observed earlier for point sources, the increase in coil's number enhances qualitatively the inversion that detects both the position and the bulk of the deposit. This is illustrated with the numerical results reported in Figure 8. Indeed, with the increase of point sources from 4, 8 to 32 points, our algorithm can locate the deposit and also gave fair approximation to its volume taken here as a semi-disk. One here wants to add as many points sources as possible to enhance the inversion and get a clearer image of

Electric conductivity in Siemens per meter (S/m)	
Vacuum	0.0
Tube	0.97E06
Deposit	1.75E06
Magnetic permeability in Henry per meter (H/m)	
Vacuum	4.0E-07 π
Tube	4.04E-07 π
Deposit	4.04E-07 π

Table 1. Physical electrical and magnetic properties of the materials used in the numerical simulations.

the deposition, although, this goes with the expenses of the computational cost mainly related to the increase in the size of the full linear system (21). It is worth noticing, although, that there is, admittedly, a limitation on the reconstruction of the deposit while increasing the number of point sources. The spread of the field generated by faraway sources could barely be detected by other faraway sources. The spread is indeed a function of the distance, the electric conductivity, and the magnetic permeability of the material where the wave travels through. A practical consideration suggests that the zone covered by the set of point sources should cover enough space susceptible to contain the deposit. For this reason, we shall consider, in our numerical experiments 32 point sources and proceed with $\tilde{\mathcal{Z}}^M$, a sparse version of the main matrix as explained above.

Examples of reconstructions obtained with $\tilde{\mathcal{Z}}^M$ for different values of M . Figure 7 presents the reconstruction of the deposit using the sparse matrix $\tilde{\mathcal{Z}}^M$ where the total scan is done with 32 point sources. In these results, we vary the number of point sources sliding along the z-direction. It is shown that this procedure, even if it dismisses some measurements (from faraway point sources) the inversion is still capable of retrieving qualitative results comparing to the use of the full matrix $\tilde{\mathcal{Z}}$, which plot is depicted in Figure 6. These promising results led us to consider the realistic case where point sources become coils-probes.

Figures 8 and 9 reproduce similar experiments to those presented in Figures 6 and 7 respectively. The outcome of the reconstruction has the same trends i.e. i) augmentation of the number of probes enhances the quality of the reconstruction and ii) the reconstruction with the limited data keeps producing good images of the deposit. Surprisingly, the case of back-scattering has produced a clear-cut image of the deposit comparable to the one obtained with the full matrix $\tilde{\mathcal{Z}}$. These promising results have challenged us to consider more complicated situations, such that including several deposits with shapes imitating the drop of water (modeling clogs).

More precisely, in Figure 10 we consider two distanced deposits with different

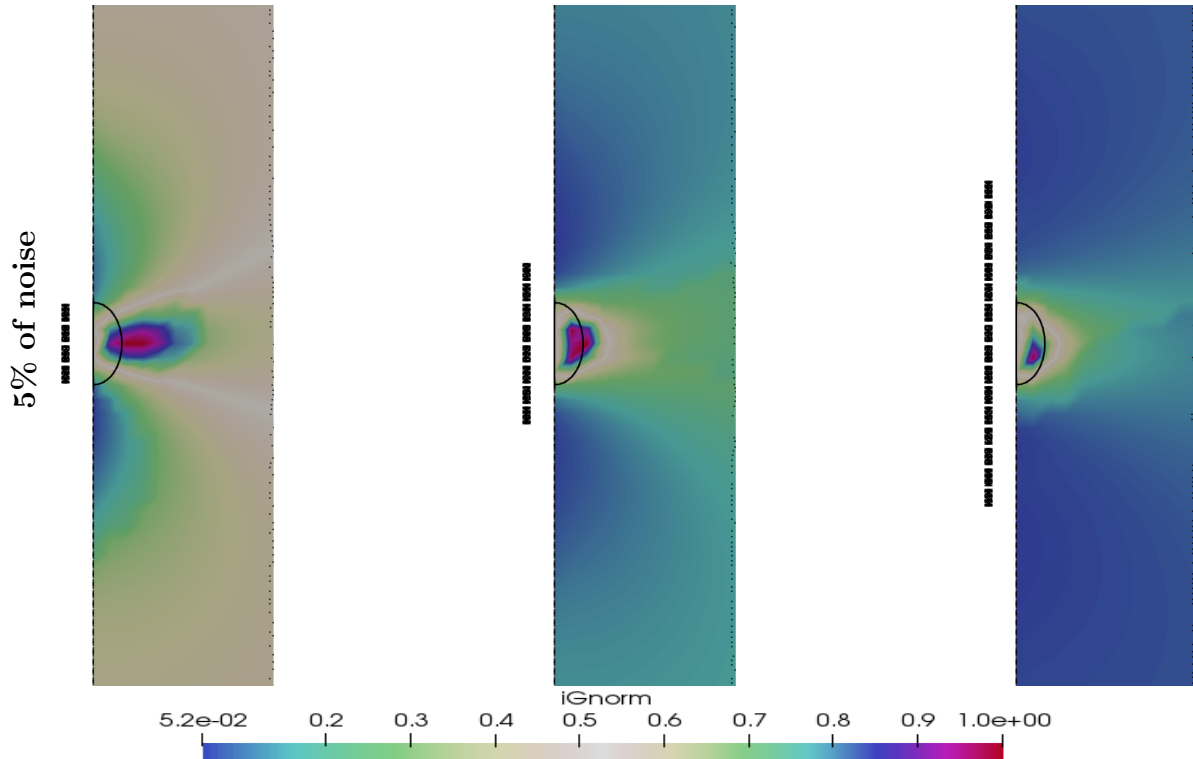


Figure 8. Reconstructions obtained for different number of coils N . From left to right, $N = 4, 8, 16$. The location of the coils is indicated with black rectangles and the exact shape of the deposit is indicated using a solid line.

shapes. The inversion algorithm is capable of detecting these two far enough deposits and performs better as the number of probes sliding along the z -direction gets increased. To illustrate the robustness with respect to noise, the same experiment as in Figure 10 is repeated in Figure 11 but with higher noise levels (20% and 40%). We cannot quantify the resolution that one may expect from our inversion algorithm but experiments shown in Figures 12 and 13 show how the performance of the inversion scheme stays reasonable as the two deposits get close to each other. Figure 14 illustrates similar conclusions. In this case, we consider a deposit with a shape that models a drop (relatively long, i.e., approximately as long as 12 coils). It is shown that the inversion algorithm can detect the bulk of the deposit and give a fair approximation of its total volume.

Conclusion

We presented in this work an eddy-current inverse shape problem and employed the so-called Linear Sampling Method to propose an imaging algorithm. We have tested and thoroughly analyzed the method both in theoretical and industrial settings, respectively. We numerically showed in particular that even for (nearly) back-scattering data, a commonly encountered configuration in practice, an adaptation of the algorithm leads to satisfying results. The latter can serve to provide fast qualitative inspection of a large

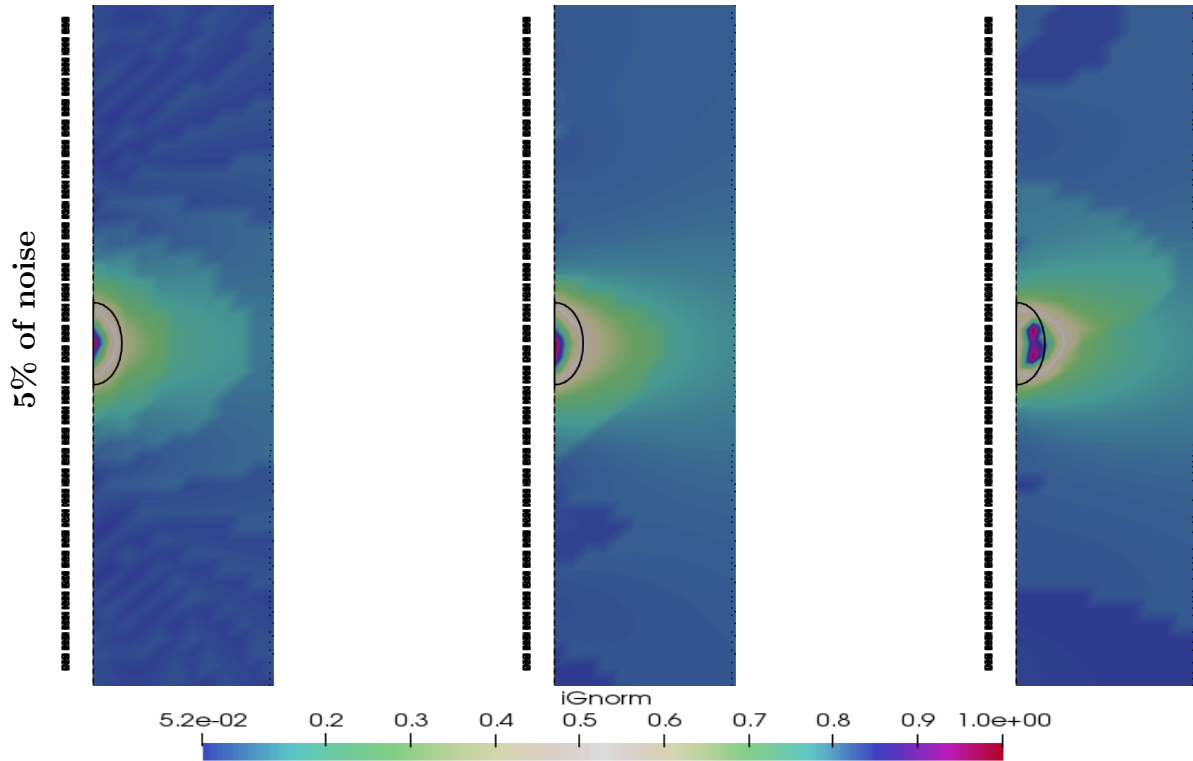


Figure 9. Reconstructions obtained with \tilde{Z}^M for different number of coils M sliding along the z -axis. From left to right, $M = 1, 2, 8$. The location that can be taken by a coil is indicated with black rectangles ($N = 32$) and the exact shape of the deposit is indicated with a solid line and it represents a semi-disc with an elliptical shape of radius 3mm in the r -direction and 5mm in the z -direction.

number of tubes. The outcome can also be used as initial guess for more computationally involved inversion methods based on optimization techniques. Exploring this coupling for 3D configurations is one of the perspectives of this work. We are also interested in studying the performance this procedure for identifying defects with different types, such as cracks hidden by deposits, which constitutes one of the main current challenges for the considered industrial application.

References

- [1] Lilian Arnold and Bastian Harrach. Unique shape detection in transient eddy current problems. *Inverse Problems*, 29(9):095004, 2013.
- [2] Franck Assous, Patrick Ciarlet Jr., and Simon Labrunie. Theoretical tools to solve the axisymmetric Maxwell equations. *Math. Methods Appl. Sci.*, 25(1):49–78, 2002.
- [3] Lorenzo Audibert, Hugo Girardon, Housseem Haddar, and Pierre Jolivet. Inversion of Eddy-Current Signals Using a Level-Set Method and Block Krylov Solvers. working paper or preprint, December 2020.
- [4] Lorenzo Audibert and Housseem Haddar. The Generalized Linear Sampling Method for limited aperture measurements. *SIAM Journal on Imaging Sciences*, 10(2):845–870, 2017.
- [5] BA Auld and JC Moulder. Review of advances in quantitative eddy current nondestructive evaluation. *Journal of Nondestructive evaluation*, 18(1):3–36, 1999.

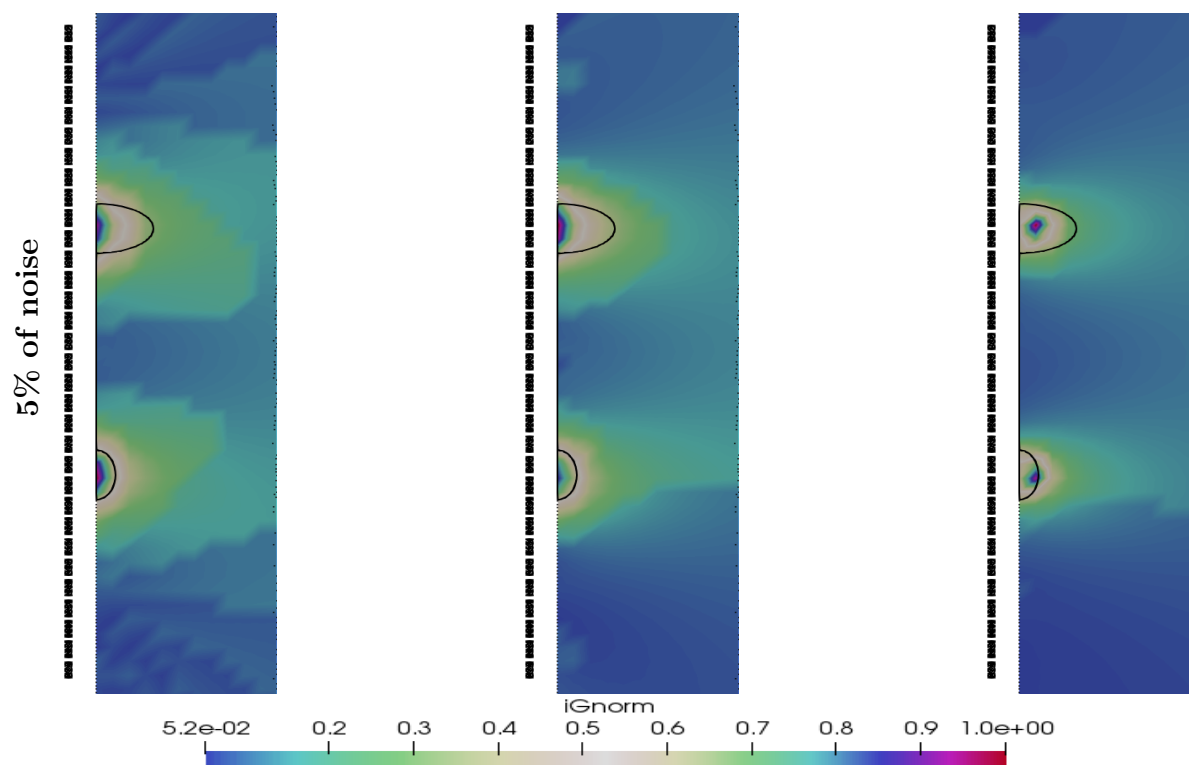


Figure 10. Reconstructions obtained with \tilde{Z}^M for different number of coils M sliding along the z -axis. From left to right, $M = 1, 2, 8$. The location that can be taken by a coil is indicated with black rectangles ($N = 32$) and the exact shape of the deposits is indicated with a solid line and it represents 2 semi-ellipses with respective semi axis = 2mm, 6mm in the r -direction and = 2mm, 3mm in the z -direction. The distance between the centers of the ellipses = 30mm.

- [6] J. Blitz. Electrical and Magnetic Methods of Non-destructive Testing, volume 2 of Non-Destructive Evaluation Series. Springer Netherlands, 1997.
- [7] Fioralba Cakoni, David Colton, and Housseem Haddar. Inverse Scattering Theory and Transmission Eigenvalues, volume 88 of CBMS Series. SIAM publications, 2016.
- [8] David Colton, Michele Piana, and Roland Potthast. A simple method using morozov's discrepancy principle for solving inverse scattering problems. Inverse Problems, 13(6):1477, 1997.
- [9] F. Dini, S. Khorasani, and R. AMROLLAHI. Green function of axisymmetric magnetostatics. Iranian Journal of Science and Technology A-Science, 28(A2), 2004.
- [10] F. Frster. Sensitive eddy-current testing of tubes for defects on the inner and outer surfaces. Non-Destructive Testing, 7(1):28 – 36, 1974.
- [11] Housseem Haddar, Zixian Jiang, and Armin Lechleiter. Artificial boundary conditions for axisymmetric eddy current probe problems. Computers and Mathematics with Applications, 68(12, Part A.):1844–1870, 2015.
- [12] Housseem Haddar, Zixian Jiang, and M. K. Riahi. A robust inversion method for quantitative 3d shape reconstruction from coaxial eddy current measurements. Journal of Scientific Computing, 70(1):29–59, 2017.
- [13] F. Hecht. New development in freefem++. Journal of Numerical Mathematics, 20(3-4):251–265, 2012.
- [14] Zixian Jiang, Mabrouka El Guedri, Housseem Haddar, and Armin Lechleiter. Eddy current tomography of deposits in steam generator. In Signal Processing Conference, 2011 19th European, pages 2054–2058. IEEE, 2011.

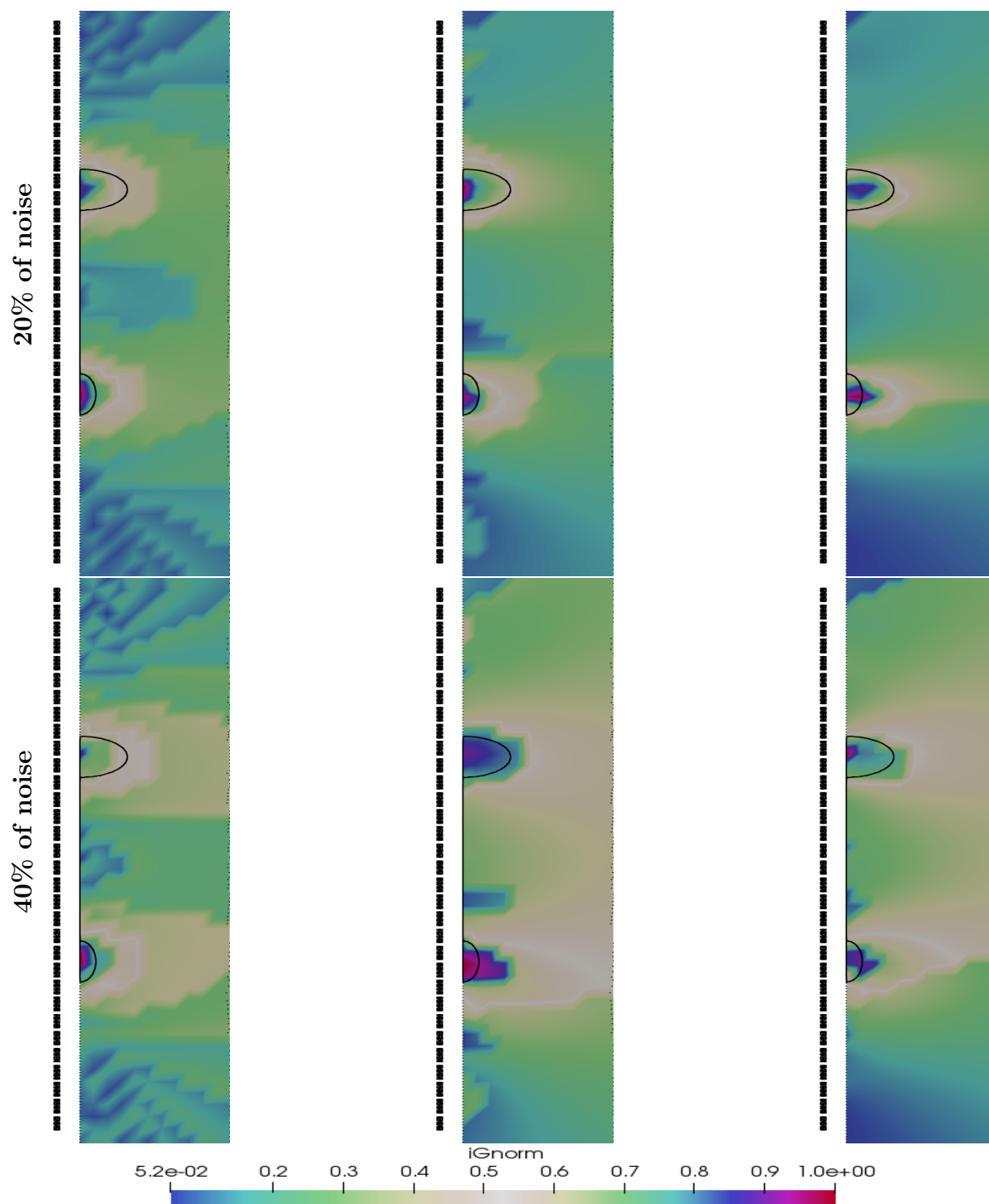


Figure 11. Reconstructions obtained for the same setting as in Figure 10 but for different noise levels (20% for the first row and 40% for the second row). The columns refer the number of coils M sliding along the z -axis. From left to right, $M = 1, 2, 8$.

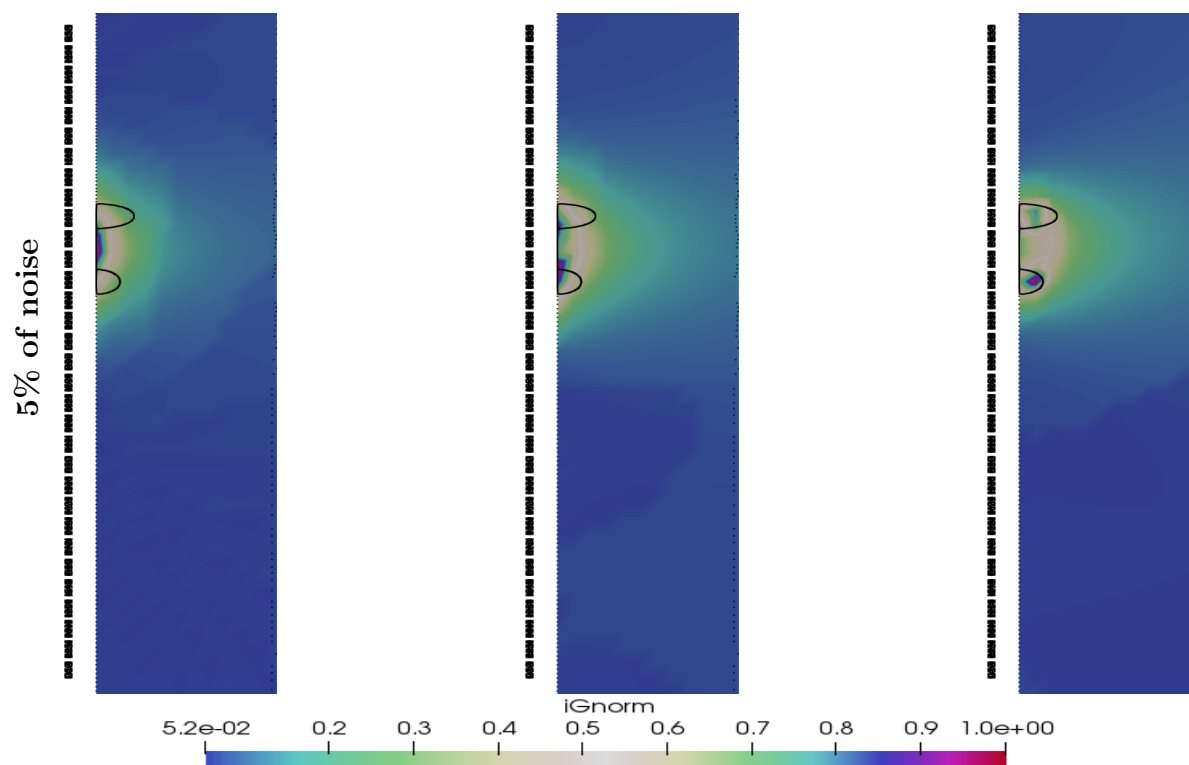


Figure 12. Reconstructions obtained for the same setting as in Figure 10. The exact shape of the deposits is indicated with a solid line and it represents 2 semi-ellipses with respective semi axis = 2mm, 2mm in the r -direction and = 1.5mm, 4mm in the z -direction. The distance between the centers of the ellipses = 8mm.

- [15] Zixian Jiang, Housseem Haddar, Armin Lechleiter, and Mabrouka El-Guedri. Identification of magnetic deposits in 2-D axisymmetric eddy current models via shape optimization. *Inverse Problems in Science and Engineering*, 2015.
- [16] Zixian Jiang, Housseem Haddar, Armin Lechleiter, and Mabrouka El-Guedri. Identification of magnetic deposits in 2-d axisymmetric eddy current models via shape optimization. *Inverse Problems in Science and Engineering*, 24(8):1385–1410, 2016.
- [17] Tariq Khan and Pradeep Ramuhalli. A recursive bayesian estimation method for solving electromagnetic nondestructive evaluation inverse problems. *IEEE Transactions on Magnetics*, 44(7):1845–1855, 2008.
- [18] Shaohua Li, Ayesha Anees, Yu Zhong, Zaifeng Yang, Yong Liu, Rick Siow Mong Goh, and En-Xiao Liu. Learning to reconstruct crack profiles for eddy current nondestructive testing, 2019.
- [19] W. McLean. *Strongly elliptic systems and boundary integral equations*. Cambridge University Press, 2000.
- [20] Gen Nakamura and Haibing Wang. Linear sampling method for the heat equation with inclusions. *Inverse Problems*, 29(10):104015, sep 2013.
- [21] Q. H. Nguyen, L. D. Philipp, D. J. Lynch, and A. F. Pardini. Steam tube defect characterization using eddy current z -parameters. *Research in Nondestructive Evaluation*, 10(4):227–252, 1998.
- [22] Touzani Rachid and Rappaz Jacques. *Mathematical Models for Eddy Currents and Magnetostatics*, volume Computational Science & Engineering. Springer Netherlands, 2014.
- [23] Mohamed Kamel Riahi. A fast eddy-current non destructive testing finite element solver in steam generator. *Journal of Coupled Systems and Multiscale Dynamics*, 4(Number 1):pp–60, 2016.
- [24] Ana Alonso Rodriguez and Alberto Valli. *Eddy Current Approximation of Maxwell Equations: Theory, Algorithms and Applications*, volume 4. Springer Science and Business Media, 2010.

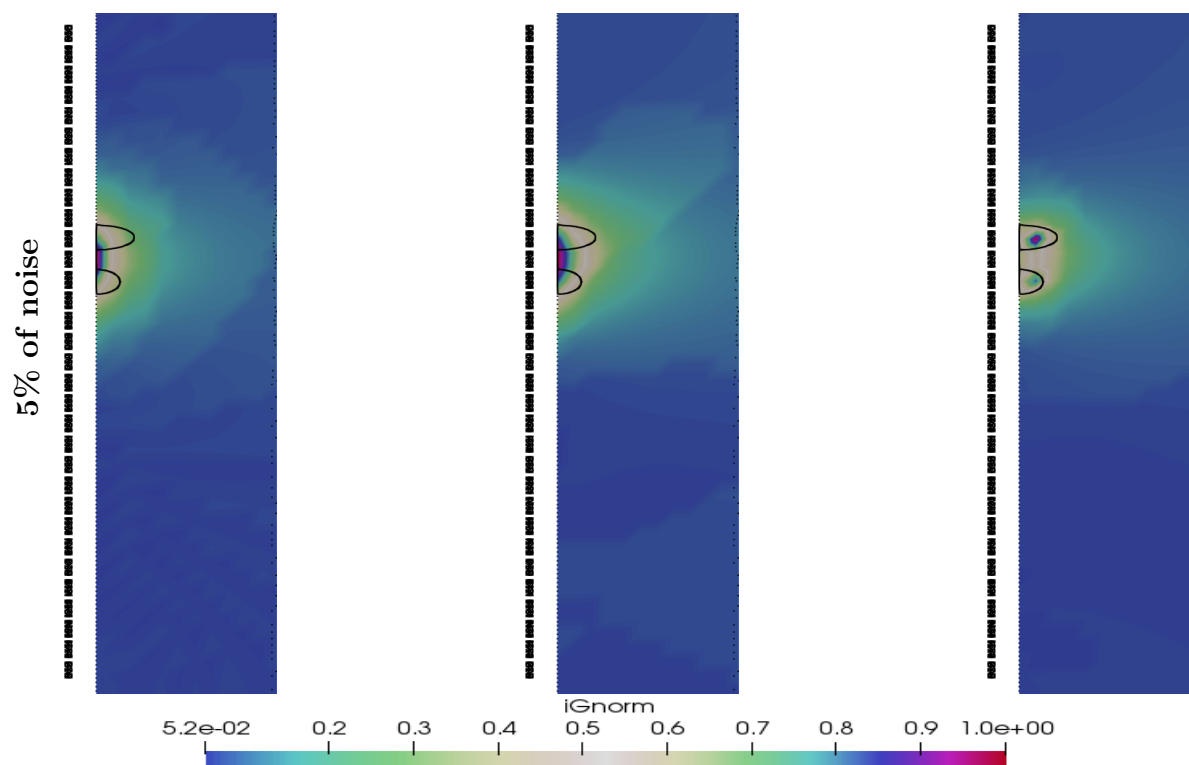


Figure 13. Reconstructions obtained for the same setting as in Figure 10. The exact shape of the deposits is indicated with a solid line and it represents 2 semi-ellipses with respective semi axis = 2mm,2mm in the r -direction and = 1.5mm, 4mm in the z -direction. The distance between the centers of the ellipses = 4mm.

- [25] Prusek T. Modélisation et simulation numérique du colmatage à l'échelle du sous-canal dans les générateurs de vapeur. PhD thesis, Université Aix-Marseille, 2012.
- [26] Antonello Tamburrino and Guglielmo Rubinacci. Fast methods for quantitative eddy-current tomography of conductive materials. IEEE transactions on magnetics, 42(8):2017–2028, 2006.

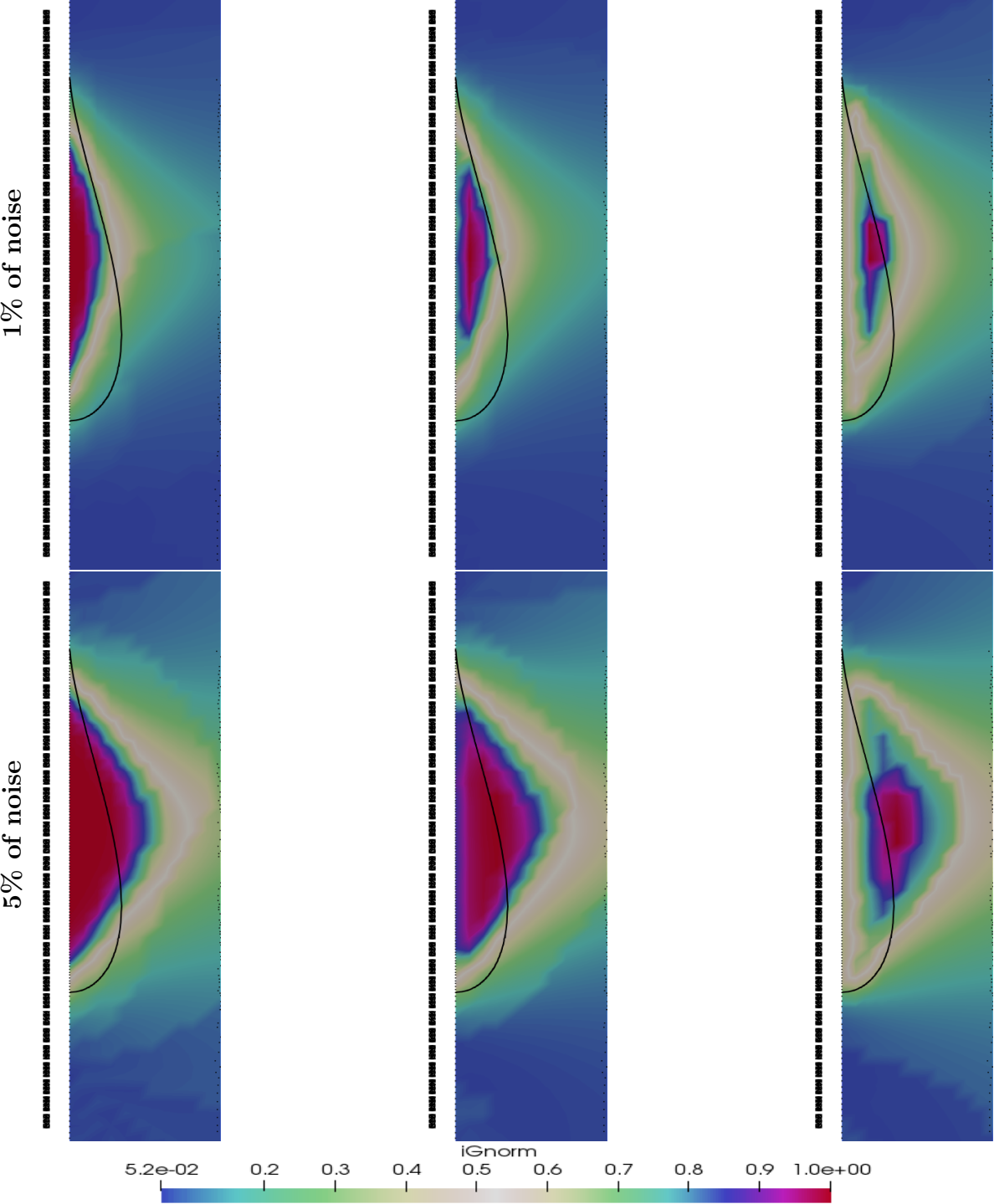


Figure 14. Reconstructions obtained with \tilde{Z}^M for different number of coils M sliding along the $z - axis$ and different noise levels. From left to right, $M = 1, 2, 8$. The location that can be taken by a coil is indicated with black small rectangle ($N = 32$) and the exact shape of the deposit is indicated with a solid line. The considered shape is about 50mm long and 8mm width.